



Article

Application of Micropore Device for Accurate, Easy, and Rapid Discrimination of *Saccharomyces pastorianus* from *Dekkera* spp.

Kazumichi Yokota ¹, Asae Takeo ², Hiroko Abe ¹, Yuji Kurokawa ², Muneaki Hashimoto ¹, Kazuaki Kajimoto ¹, Masato Tanaka ¹, Sanae Murayama ³, Yoshihiro Nakajima ¹, Masateru Taniguchi ³ and Masatoshi Kataoka ^{1,*}

- ¹ Health and Medical Research Institute, National Institute of Advanced Industrial Science and Technology (AIST), 2217-14 Hayashi-cho, Takamatsu, Kagawa 761-0395, Japan; kazumichi-yokota@aist.go.jp (K.Y.); abe-abe@aist.go.jp (H.A.); muneaki-hashimoto@aist.go.jp (M.H.); k-kajimoto@aist.go.jp (K.K.); mst-tanaka@aist.go.jp (M.T.); y-nakajima@aist.go.jp (Y.N.)
- ² Institute for Future Beverages, Research & Development Division, Kirin Holdings Company, Limited. 1-17-1, Namamugi, Tsurumi-ku, Yokohama, Kanagawa 230-8628, Japan; Asae_Takeo@kirin.co.jp (A.T.); y-kurokawa@kirin.co.jp (Y.K.)
- ³ The Institute of Scientific and Industrial Research, Osaka University, 8-1 Mihogaoka, Ibaraki, Osaka 567-0047, Japan; murayama@sanken.osaka-u.ac.jp (S.M.); taniguti@sanken.osaka-u.ac.jp (M.T.)
- * Correspondence: m-kataoka@aist.go.jp; Tel.: +81-87-869-3576

Abstract: Traceability analysis, such as identification and discrimination of yeasts used for fermentation, is important for ensuring manufacturing efficiency and product safety during brewing. However, conventional methods based on morphological and physiological properties have disadvantages such as time consumption and low sensitivity. In this study, the resistive pulse method (RPM) was employed to discriminate between *Saccharomyces pastorianus* and *Dekkera anomala* and *S. pastorianus* and *D. bruxellensis* by measuring the ionic current response of cells flowing through a micro-sized pore. The height and shape of the pulse signal were used for the simultaneous measurement of the size, shape, and surface charge of individual cells. Accurate discrimination of *S. pastorianus* from *Dekkera* spp. was observed with a recall rate of $96.3 \pm 0.8\%$. Furthermore, budding *S. pastorianus* was quantitatively detected by evaluating the shape of the waveform of the current ionic blockade. We showed a proof-of-concept demonstration of RPM for the detection of contamination of *Dekkera* spp. in *S. pastorianus* and for monitoring the fermentation of *S. pastorianus* through the quantitative detection of budding cells.

Keywords: resistive pulse method; yeast; discrimination; brewer; *Saccharomyces pastorianus*; *Dekkera* spp.



Citation: Yokota, K.; Takeo, A.; Abe, H.; Kurokawa, Y.; Hashimoto, M.; Kajimoto, K.; Tanaka, M.; Murayama, S.; Nakajima, Y.; Taniguchi, M.; et al. Application of Micropore Device for Accurate, Easy, and Rapid Discrimination of *Saccharomyces pastorianus* from *Dekkera* spp.. *Biosensors* **2021**, *11*, 272. <https://doi.org/10.3390/bios11080272>

Received: 19 July 2021

Accepted: 7 August 2021

Published: 12 August 2021

Publisher's Note: MDPI stays neutral with regard to jurisdictional claims in published maps and institutional affiliations.



Copyright: © 2021 by the authors. Licensee MDPI, Basel, Switzerland. This article is an open access article distributed under the terms and conditions of the Creative Commons Attribution (CC BY) license (<https://creativecommons.org/licenses/by/4.0/>).

1. Introduction

The resistive pulse method (RPM) is used for evaluating the transient ionic current blockade associated with the translocation of individual nano- to micro-sized particles passing through an appropriate diameter pore. Moreover, it is applicable in proving small objects by using pulse-like electrical signals. In addition, because the measured ionic current blockade signals possess information regarding the properties of these particles such as size [1], shape [2–4], surface charge [1,5], and deformability [6,7], these objects can be discriminated at a single-particle resolution. Further, single bioparticles of various sizes ranging from blood cells to polynucleotides can be discriminated against without implementing immunostaining [2,8,9]. RPM with micro-sized pores (micropore devices), which is similar to the operating principles of a Coulter counter, is widely used to measure the number of blood cells in hematological diagnosis.

In brewing, traceability analysis such as identification and/or discrimination of microorganisms used for fermentation is important to ensure manufacturing efficiency and

product safety [10,11]. The genus *Saccharomyces* is well-known as the key yeast species in beer fermentation, and *S. pastorianus* is used in bottom-fermented beer [12]. Although the presence of *Brettanomyces* yeasts (teleomorph *Dekkera*) including *Dekkera anomala* and *D. bruxellensis* is encouraged in several types of beer, these yeasts cause contaminations of most beer leading to spoilage [12,13].

Conventional methods used for the detection and/or isolation of yeast contamination are based mainly on morphological and physiological properties [14]. Several types of selective media are commonly used to identify and discriminate unknown yeasts. However, these cultivation methods require several days to obtain results. Although gene analysis methods based on PCR are also employed to identify and/or discriminate brewing yeasts [14,15], some disadvantages remain. For example, several hours are required to acquire results and complex operations. Therefore, detection methods for unwanted yeast contamination in brewing with rapid and easy operation, such as in-line inspection, are necessary.

In this study, we developed a micropore device for the accurate and rapid discrimination of *S. pastorianus* from *Dekkera* spp. The budding state of *S. pastorianus* can also be detected at the single-cell level by analyzing the shape of the current blockade signals.

2. Materials and Methods

2.1. Yeast Strains and Preparation

S. pastorianus W34/70, *D. anomala* DSMZ 70727, and *D. bruxellensis* NBRC 0677 were used in this study. These yeasts were cultivated in YPAD agar plates [16] (Thermo Fisher Scientific, Inc., Waltham, MA, USA) for at least 2 days. To prepare the cell sample solution for ionic current measurements, appropriate amounts of each yeast were collected from a single colony and suspended in 50 mM 2-(N-morpholino) ethanesulfonic acid (MES) buffer to a concentration of 1×10^6 cells/mL.

2.2. Cell Size Measurement Using Light Microscope

One hundred cells in each cell suspension in 50 mM MES buffer were selected using a light microscope (DIML II, Leica Camera AG, Wetzlar, Germany) with a 40 \times objective lens to determine each yeast size. Approximately 20 μ L of each cell sample was seeded into a 96-well plate (Nunc MicroWell 96-Well Microplates, Thermo Fisher, Inc.) to settle at the bottom of the plate surface, and the diameter of each cell was measured immediately [Figure 1a–c]. Cell sizes were expressed as mean \pm standard deviation (SD).

2.3. Micropore Device and Ionic Current Measurement

For the ionic current measurement of cells, we employed a micropore device with a diameter of 10 μ m and thickness of 50 nm, as shown in Figure 1d (M-NK-1000-A106-001-Pm, Aipore, Inc., Tokyo, Japan). Then, 10 μ L of cell sample solution was injected into the cathode-side microchamber through the inlet, and 10 μ L of 50 mM MES buffer was injected into the anode-side microchamber through the inlet. For cell mixture measurement, two of three types of yeast, 5 μ L each and 10 μ L in total, were injected into the cathode-side microchamber.

A current amplifier (ACDC3000, AXIS NET, Inc., Osaka, Japan) was employed for ionic current measurement in the current range of 2.5 μ A using the LabVIEW (LabVIEW 2017, National Instruments, Austin, TX, USA) program. The time trace of the ionic current was evaluated via the pore and was recorded at a sampling rate of 1 MHz using a voltage input module (NI-9223, National Instruments), which corresponds to a 1- μ s resolution time. Typical waveforms of the ionic current blockade for *S. pastorianus*, *D. anomala*, and *D. bruxellensis* are shown in Figure 1e–g. The duration of the blockade signal was >0.2 ms, and the employed sampling rate was sufficient to analyze the signal of the current blockade. For each experiment, 400 current blockade signals could be obtained in 6 min.

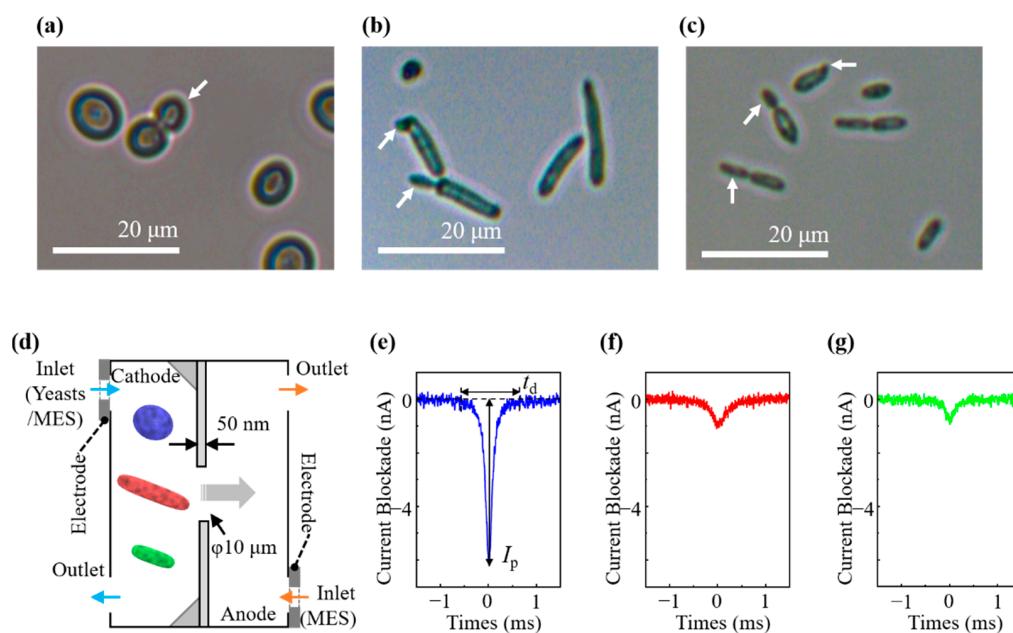


Figure 1. Light microscopic images of (a) *S. pastorianus*, (b) *D. anomala*, and (c) *D. bruxellensis*. Budding is observed in each. Arrows indicate daughter cells. (d) Picture of micropore device with a diameter of 10 μm . A typical waveform of current ionic blockade by RPM was observed for (e) *S. pastorianus*, (f) *D. anomala*, and (g) *D. bruxellensis*.

2.4. Resistive Pulse Analysis and Cell Discrimination

We measured resistive pulse signals that appeared on the time trace of the ionic current by monitoring the current displacement, which was larger than the threshold by three times the SD. Further, we averaged the data for the nearest neighboring points to reduce the current noise in the pulse measurement process, as reported by Smeets et al. [17]. In addition, we extracted the waveforms of the pulses of the original 1-MHz data at the time point of pulse detection and evaluated the peak values of the current blockade (I_p) and the duration of the current blockades (t_d) on the extracted waveform [Figure 1e–g]. Four hundred pulse signals were analyzed. These data were processed using LabVIEW.

2.5. Discrimination of Decision Boundary and Discrimination Error

Compared with the linear separation boundary [18], a quadratic discrimination analysis (QDA) with a nonlinear separation boundary can discriminate more accurately between different classes. QDA is a probabilistic parametric classification technique that separates the class region by quadratic boundaries assuming that each class has a multivariate normal distribution with the dispersion being different per class. The decision boundary (DB) by QDA for cell discrimination is defined by a contour line/curve providing an equal probability of the I_p , t_d , and I_p - t_d distributions for each cell [19,20]. The probability is expressed as follows:

$$P(\log_{10} y) = \frac{1}{\sqrt{2\pi|\Sigma_k|}} \exp\left(-\frac{1}{2}(\log_{10} y - \langle \log_{10} y \rangle_k)^T \Sigma_k^{-1} (\log_{10} y - \langle \log_{10} y \rangle_k)\right).$$

where Σ_k and $\langle \log_{10} y \rangle_k$ are the variance-covariance matrix and the mean value of observations $\log_{10} y$ for the k th dimension ($k = \log_{10} I_p$ or $\log_{10} t_d$), respectively.

2.6. Zeta Potential Measurement

The zeta potential was measured using a zeta potential analyzer (ELSZ-2000Z Otsuka Electronics Co., Ltd., Osaka, Japan). A glass flow cell for measurements was filled with 1.0 mL of cell sample at a concentration of 1×10^8 cells/mL in 50 mM MES buffer. While

applying an electric field of ~ 16 V/cm on average, the electrical mobility was evaluated from the Doppler shift of the scattering light of the laser, and the zeta potential ζ was obtained by fitting the electrophoretic velocity of cells flow inside the measurement glass cell based on the Smoluchowski equation [21]. The measured zeta potential is represented by the mean \pm SD ($n = 6$).

2.7. Multiphysics Simulations of Ionic Current Waveform for a Budding Yeast

To elucidate the characteristic ionic current waveforms originating from the morphological features of budding yeasts passing through a pore, numerical simulations based on finite element methods were conducted [2,4]. The geometric structures were modeled in a cylindrical coordinate system (r , θ , and z as the radial, azimuthal, and axial coordinates, respectively), as shown in Figure 4a. The total model size was $50 \mu\text{m}$ in radius ($R = 50 \mu\text{m}$) and $100 \mu\text{m}$ in z -height. A membrane with a thickness of 50 nm formed a $5\text{-}\mu\text{m}$ radius pore [white arrow in Figure 4a] and was placed in the middle of the model ($z = 0 \mu\text{m}$).

A yeast model [black arrow in Figure 4a] of a given size (parameterized by L_x) was positioned along the z -axis. The multiphysics simulation was conducted by simultaneously solving Equation (1) the continuity equation at a steady-state ($\nabla \cdot j = 0$, where j is the current density) for the applied electric potential of V_c , Equation (2) the Poisson–Boltzmann equation for the electrostatic potential of V_s , Equation (3) the Nernst–Planck equation for the i ion concentration of c_i , and Equation (4) the incompressible Navier–Stokes equation for the hydrodynamic pressure and the flow field of p and U :

$$\nabla \cdot j = \nabla \cdot \left[- \left(\sigma_w + F \sum_i z_i^2 u_i c_i \right) \nabla V_c \right] = 0 \quad (1)$$

$$\nabla^2 V_s = - \frac{\rho}{\epsilon_w} = - \frac{1}{\epsilon_w} F \sum_i z_i c_i \exp(-z_i e V_s / k_B T) \quad (2)$$

$$\nabla \cdot (-D_i \nabla c_i - z_i u_i F c_i \nabla V_s) + U \cdot \nabla c_i = 0 \quad (3)$$

$$- \nabla p + \eta \nabla^2 U - \rho \nabla V_c = 0 \quad (4)$$

Here, σ_w , F , z_i , and u_i are the electrical conductivity of water, the Faraday constant, charge number, and electrical mobility of ion i , respectively. We used $z_i = 1$ and $u_i = 3.69 \times 10^{-7} \text{ m}^2/\text{V}\cdot\text{s}$ for $i = \text{H}^+$, and $z_i = -1$ and $u_i = 2.87 \times 10^{-8} \text{ m}^2/\text{V}\cdot\text{s}$ for $i = \text{MES}^-$. These u_i values were evaluated from the diffusion coefficient of D_i [22,23] based on the Einstein relation $u_i = eD_i/k_B T$, where e , k_B , and T are the elementary charge, Boltzmann constant, and temperature, respectively. ρ , ϵ_w , and η are the net ionic charge density, permittivity, and dynamic viscosity of water, respectively.

The boundary conditions for Equation (1) [V_c at $z = 50 \mu\text{m}$ and $-50 \mu\text{m}$] were 0.1 V and 0 V , respectively. For Equation (2), a surface charge of $-0.015 \text{ C}/\text{m}^2$, estimated from the zeta potential by using the Grahame equation [24,25], was imposed on the surfaces of the pore and the yeast model. For Equation (3), the boundaries at $z = \pm 50 \mu\text{m}$ and $r = 50 \mu\text{m}$ were assumed to be $c_i = 2.6 \text{ mM}$. This c_i value was estimated based on the assumption that the total ionic current was 100 nA , which corresponded to the experimentally measured baseline current. The other boundary conditions were similar to those in a previous study [2].

The resulting electric potential ($V_c + V_s$) distribution is shown in Figure 4a. The total ionic current I was calculated by the surface integral for j in the z -direction (j_z) at $z = 50 \mu\text{m}$ over the r - θ surface, expressed as

$$I = \int_0^R r dr \int_0^{2\pi} d\theta j_z \quad (5)$$

All numerical simulations were performed with COMSOL Multiphysics 5.0 (COMSOL, Inc., Stockholm, Sweden) using the physical parameters of $\sigma_w = (18.2 \text{ M}\Omega\cdot\text{cm})^{-1}$,

$F = 9.649 \times 10^4 \text{ C/mol}$, $e = 1.602 \times 10^{-19} \text{ C}$, $k_B = 1.381 \times 10^{-23} \text{ J/K}$, $T = 293.15 \text{ K}$, $\epsilon_w = 7.097 \times 10^{-10} \text{ F/m}$, and $\eta = 1.002 \times 10^{-3} \text{ Ns/m}^2$ [23].

3. Results and Discussion

3.1. Morphological Examination by Light Microscopy

Light microscopic images of cells are shown in Figure 1a–c. *S. pastorianus* cells were round to ovoid shapes with a size of $5.6 \pm 0.9 \times 6.9 \pm 1.2 \mu\text{m}$ [Figure 1a]. Both *D. anomala* and *D. bruxellensis* were spindle-shaped at $2.9 \pm 0.8 \times 13.6 \pm 5.7 \mu\text{m}$ and $2.5 \pm 0.5 \times 7.9 \pm 3.2 \mu\text{m}$, respectively [Figure 1b,c]. The size and shape of *S. pastorianus* were clearly different from those of *D. anomala* and *D. bruxellensis*. Budding was observed in some cells [Figure 1a–c].

3.2. Ionic Current Measurement of Cells and Cell Discrimination

We applied a bias voltage of $V_b = 0.1 \text{ V}$ between the cathode-side and the anode-side microchambers, and the baseline had a current level of approximately 100 nA. The electrical conductivity (σ) was determined to be $0.104 \pm 0.06 \text{ S/m}$. The electric field generated by the bias voltage yields electric forces that drive the cells and translate them through the pores. As illustrated in Figure 1d, the cells were restricted by a pore, causing them to pass turn by turn through the pore, thus yielding a one-to-one correspondence of a pulselike signal between the ionic current blockade and a translocation event of a cell through the pore.

Figure 1e–g depict typical waveforms of the current blockades generated by *S. pastorianus*, *D. anomala*, and *D. bruxellensis*, respectively. The size and deformability of the sensed particles were estimated from the I_p values generated by the RPM [1,6,7]. The I_p values of *S. pastorianus*, *D. anomala*, and *D. bruxellensis* were $6.16 \pm 3.96 \text{ nA}$, $0.99 \pm 0.58 \text{ nA}$, and $0.75 \pm 0.46 \text{ nA}$, respectively, which are significantly different. t_d can be utilized to elucidate the surface charge of the sensed particles [1,5]. The zeta potential was examined to estimate the surface charge of the cells. The evaluated zeta potentials for *S. pastorianus*, *D. anomala*, and *D. bruxellensis* were $-28.99 \pm 0.50 \text{ mV}$, $-16.50 \pm 0.64 \text{ mV}$, and $-14.42 \pm 0.90 \text{ mV}$, respectively. Contrary to the prediction from the results of zeta potential measurement, the t_d values were $1.31 \pm 0.89 \text{ ms}$, $1.07 \pm 1.12 \text{ ms}$, and $0.93 \pm 0.90 \text{ ms}$ with statistical differences between *S. pastorianus*, *D. anomala*, and *D. bruxellensis*, respectively. Since the I_p values for *Dekkera* spp. are extremely smaller than that of *S. pastorianus*, it is considered that *Dekkera* spp. pass through the pore with a longitudinal direction. The minor axis of *Dekkera* spp. is less than half that of *S. pastorianus*, and the spindle-shaped *Dekkera* spp. are thought to be more mobile than the round shape of *S. pastorianus* in solution, so it may be faster to pass the pore [26]. Therefore, it may be that the t_d values indicating the residence time in the pore becomes shorter in long *Dekkera* spp. compared with short *S. pastorianus*.

The reproducibility of I_p and t_d measurements by the RPM for these yeasts was confirmed by three different experiments [27] [Figure 2a]. The histogram of I_p on log, t_d on log, and scatter plot of I_p – t_d on log–log, and the BDs for each cell are shown in Figure 2b. If cells are present in regions I, II, and III on each graph, then they are estimated as *D. bruxellensis*, *D. anomala*, and *S. pastorianus*, respectively. The electrical current records and I_p – t_d scatter plot by RPM of a mixture of two types of yeast from *S. pastorianus*, *D. anomala*, and *D. bruxellensis* are shown in Figure 3. Large variations in current blockade were observed in each mixture of *S. pastorianus* and *D. anomala* [Figure 3a], and *S. pastorianus* and *D. bruxellensis* [Figure 3b]. Relatively uniform small current blockades could be observed in the mixture of *D. anomala* and *D. bruxellensis* [Figure 3c]. The cell distribution on the I_p – t_d scatter plot by RPM analysis of cell mixture and single measurement [Figure 2b] is very similar and has high applicability of RPM for accurate discrimination of *S. pastorianus* from *Dekkera* spp. can be expected.

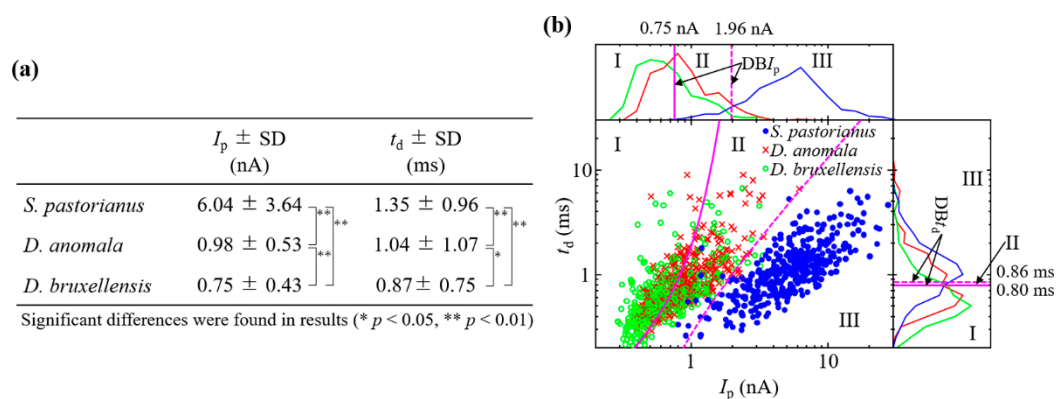


Figure 2. Reproducibility of I_p and t_d measurement by RPM for (a) *S. pastorianus*, *D. anomala*, and *bruxellensis*. (b) Histogram of I_p on log, t_d on log, I_p - t_d on log-log, and DBs for *S. pastorianus*, *D. anomala*, and *D. bruxellensis*.

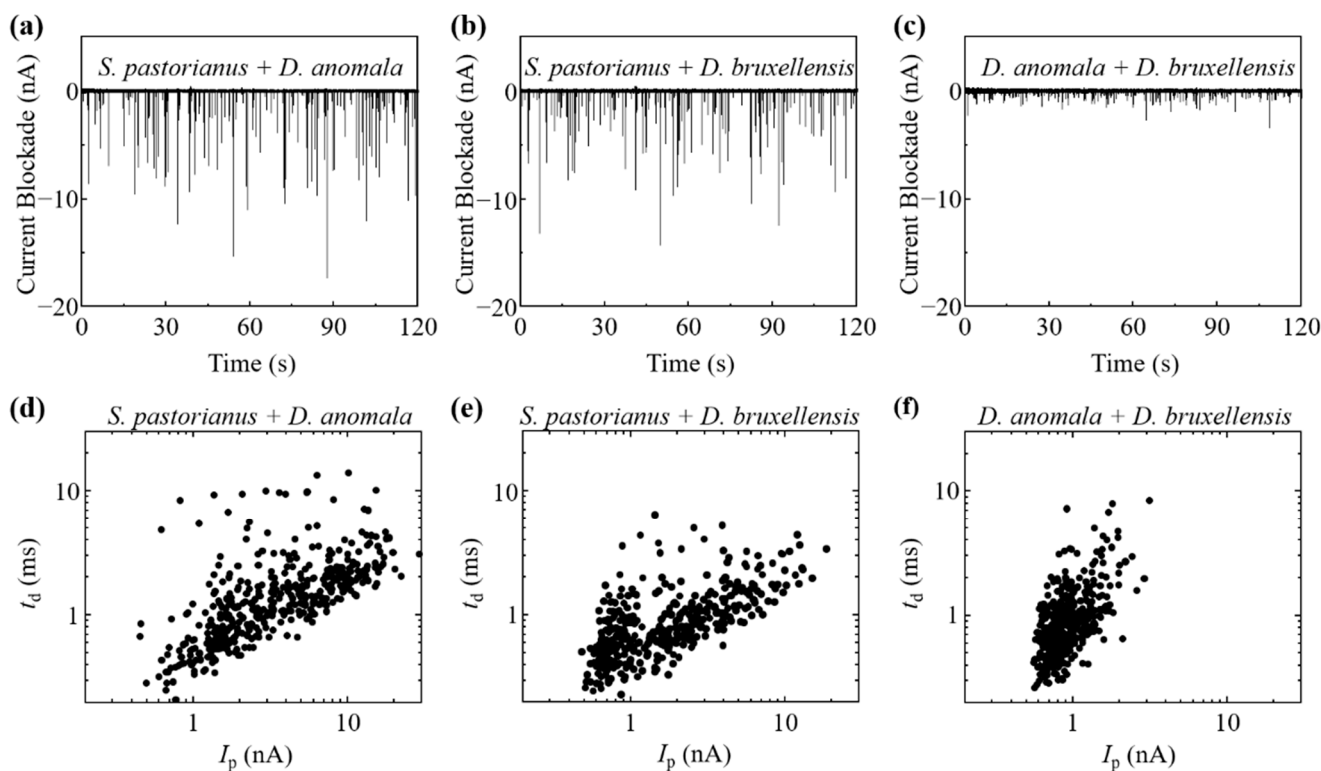


Figure 3. Electrical current record by RPM of each mixture of (a) *S. pastorianus* and *D. anomala*, (b) *S. pastorianus* and *D. bruxellensis*, and (c) *D. anomala* and *D. bruxellensis*. I_p - t_d scatter plot on log-log graph by RPM of each mixture of (d) *S. pastorianus* and *D. anomala*, (e) *S. pastorianus* and *D. bruxellensis*, and (f) *D. anomala* and *D. bruxellensis*.

Recall rates of *S. pastorianus*, *D. anomala*, and *D. bruxellensis* were estimated on $\log_{10}I_p$ to be $92.4 \pm 1.9\%$, $54.5 \pm 5.3\%$, and $62.6 \pm 3.1\%$, respectively [Figure 2b and Table 1]. *S. pastorianus* was detected with high sensitivity. On the other hand, recall rates of *S. pastorianus*, *D. anomala*, and *D. bruxellensis* were estimated to be $56.8 \pm 8.9\%$, $19.5 \pm 13.2\%$, and $66.8 \pm 5.4\%$ on $\log_{10}t_d$, respectively. Highly sensitive detection of *S. pastorianus* was not observed. By performing discriminant analysis on the $\log_{10}I_p$ - $\log_{10}t_d$ plane, a significant improvement in the recall rate for *S. pastorianus* was $96.3 \pm 0.8\%$ compared to $\log_{10}I_p$ and $\log_{10}t_d$ (McNemar test, $p < 0.05$). The limit of detection was 2.4%, which gave a signal at 3SDs above the backgrounds. The accuracy of *S. pastorianus* identification by PCR is reported to be 94.6% [12]. RPM can be expected to be as accurate as PCR. These

results indicate the potential of I_p-t_d analysis by RPM for the quantitative detection of *S. pastorianus* in solution and the accurate detection of *Dekkera* spp. contamination.

Table 1. Discrimination of investigated yeasts based on $\log_{10}I_p$ acquired by RPM.

		Predicted Classification			
		<i>S. pastorianus</i>	<i>D. anomala</i>	<i>D. bruxellensis</i>	Total
Actual classification	<i>S. pastorianus</i>	376	22	2	400
		372	28	0	400
		361	39	0	400
	Recall	92.4 ± 1.9%			
	<i>D. anomala</i>	19	242	139	400
		25	209	166	400
		23	203	174	400
	Recall	54.5 ± 5.3%			
	<i>D. bruxellensis</i>	10	138	252	400
		10	128	262	400
8		155	237	400	
Recall	62.6 ± 3.1%				
Discrimination of investigated yeasts based on $\log_{10}t_d$ acquired by RPM.					
		Predicted Classification			
		<i>S. pastorianus</i>	<i>D. anomala</i>	<i>D. bruxellensis</i>	Total
Actual classification	<i>S. pastorianus</i>	204	88	108	400
		268	15	117	400
		209	32	159	400
	Recall	56.8 ± 8.9%			
	<i>D. anomala</i>	100	106	194	400
		178	17	205	400
		113	111	176	400
	Recall	19.5 ± 13.2%			
	<i>D. bruxellensis</i>	73	80	247	400
		97	13	290	400
101		34	265	400	
Recall	66.8 ± 5.4%				
Discrimination of investigated yeasts based on $\log_{10}I_p-\log_{10}t_d$ acquired by RPM.					
		Predicted Classification			
		<i>S. pastorianus</i>	<i>D. anomala</i>	<i>D. bruxellensis</i>	Total
Actual classification	<i>S. pastorianus</i>	383	15	2	400
		389	11	0	400
		384	14	2	400
	Recall	96.3 ± 0.8%			
	<i>D. anomala</i>	11	252	137	400
		12	247	141	400
		5	243	152	400
	Recall	61.8 ± 1.1%			
	<i>D. bruxellensis</i>	3	139	258	400
		4	139	257	400
1		62	337	400	
Recall	71.0 ± 11.5%				

3.3. Analysis of Budding *S. pastorianus*

In the RPM analysis for *S. pastorianus*, 87.6% of the waveforms [Figure 4b, blue] were symmetrical, and 11.8% had shoulders before the peak time [Figure 4b, cyan] of the waveform and 0.6% after [Figure 4b, purple]. As shown in Figure 1a, budding was observed in some cells. Budding was observed in 11.9% of *S. pastorianus* on microscopic images (data not shown), which is close to the appearance rate of the shoulder-shaped waveform in the RPM.

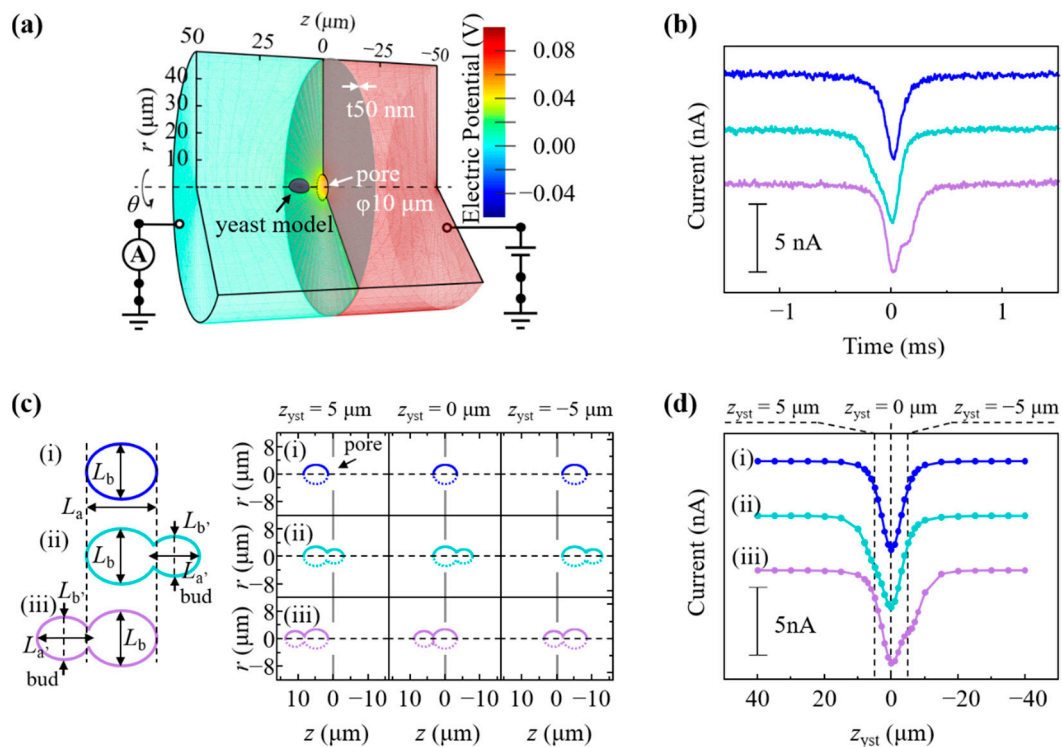


Figure 4. (a) Geometric structure modeled in a cylindrical coordinate system. r , θ , and z indicate coordinate, azimuthal angle, and axial coordinate, respectively. The color scale at the right represents the electric potential. (b) Measured symmetric waveform (blue), waveform with the shoulder before peak time (cyan), and waveform with a shoulder after peak time (purple). (c) Simulated model of passing through the pore of the nonbudding cell (i) and budding cell with daughter in front of (ii) or behind (iii) mother cell. (d) Simulated waveforms of the nonbudding cell (i), budding cell with daughter in front of (ii) or behind (iii) mother cell.

We simulated whether the shoulder shape of the waveform shows budding by using multiphysics simulations. The size parameter L_x for the yeast model is a variable that defines the distribution of V_c , V_s , c_i , p , and U , including j and ρ in Equations (1)–(4), and affect I in Equation (5) [28,29]. In Figure 4c, the blue ellipsoid with $L_a = 6.9 \mu\text{m}$ on the major axis and $L_b = 5.6 \mu\text{m}$ on the minor axis represents a nonbudding *S. pastorianus* (i). The budded *S. pastorianus* (cyan and purple) was modeled by merging a bud (daughter cell) to the forward and backward of the mother cell (ii and iii). The sizes of the mother cell (L_a and L_b) and those of daughter cells ($L_{a'} = 5.0 \mu\text{m}$ and $L_{b'} = 4.1 \mu\text{m}$ for cyan, and $L_{a'} = 5.6 \mu\text{m}$ and $L_{b'} = 4.5 \mu\text{m}$ for purple) were assumed from the microscopic images. Figure 4d shows the change in I during the yeast z -position displacement of $z_{\text{yst}} = 40$ to $-40 \mu\text{m}$. The peak of the current blockade appeared at $z_{\text{yst}} = 0 \mu\text{m}$ [Figure 4d, i–iii]. The gap of the pore by passing through cells was minimized in the cell model size of L_a and L_b at $z_{\text{yst}} = 0 \mu\text{m}$ [Figure 4c, i–iii]. In contrast to the symmetric shape of (d, i), the shoulder appeared at $z_{\text{yst}} > 0$ for (d, ii) and $z_{\text{yst}} < 0$ for (d, iii). These corresponded to the passage of the budded *S. pastorianus* model through the pore in the order of daughter-parent (c, ii) or parent-daughter (c, iii), and the appearance of the shoulder was related

to the daughter cell size. The simulated waveforms [Figure 4d] were in good agreement with the experimentally measured waveforms [Figure 4b]. Budding *S. pastorianus* can be quantitatively detected by measuring the shouldered waveform of the current ionic blockade. The contributions of the size and orientation of yeasts to the waveform can explain the RPM for the investigated *Dekkera* spp., in which clear shoulders were not seen. *Dekkera* spp. has an elongated spindle shape, and the major axis of *D. anomala* is larger than the pore diameter [Figure 1b,c]. This restricts the orientation of those during passage through the pore in the longitudinal direction, and the cell passes through the pores with its major axis parallel to the z-axis. Since the minor axis of *Dekkera* spp. is apparently smaller than that of *S. pastorianus* [Figure 1a–c], their obtained I_p values obtained are smaller than those of *S. pastorianus* [Figure 1e–g]. The current resolution to discriminate the budding cells in *Dekkera* spp. may be insufficient by the RPM analysis employed in this study. A smaller-sized pore is necessary to improve the resolution for analyzing the budding of *Dekkera* spp. These results indicate the potential application of RPM for the monitoring of growth viability and fermentation of yeasts by the quantitative detection of budding cells [30–32].

4. Conclusions

In this study, we demonstrated the potential of RPM analysis using a micropore device with a 10- μ m diameter pore for accurate discrimination of *S. pastorianus* from *Dekkera* spp. by measuring multiple parameters such as cell size, and the quantitative detection of budding *S. pastorianus* by evaluating the shape of the waveform of the current ionic blockade. We demonstrated the proof-of-concept of RPM for the detection of *Dekkera* spp. contamination in *S. pastorianus* and for monitoring the fermentation of *S. pastorianus* through the quantitative detection of budding cells.

Author Contributions: K.Y., A.T., H.A., Y.K., M.H., K.K., Y.N. and M.K. designed and conducted the experiments. M.T. (Masato Tanaka), S.M. and M.T. (Masateru Taniguchi) constructed the measurement system and designed the micropore device. K.Y. and M.K. wrote the manuscript. All authors have read and agreed to the published version of the manuscript.

Funding: This work was supported by JSPS KAKENHI grant number 19H04495.

Institutional Review Board Statement: Not applicable.

Informed Consent Statement: Not applicable.

Data Availability Statement: Not applicable.

Conflicts of Interest: The authors declare no conflict of interest.

References

1. Song, Y.; Zhang, J.; Li, D. Microfluidic and Nanofluidic Resistive Pulse Sensing: A Review. *Micromachines* **2017**, *8*, 204. [[CrossRef](#)]
2. Tsutsui, M.; Yoshida, T.; Yokota, K.; Yasaki, H.; Yasui, T.; Arima, A.; Tonomura, W.; Nagashima, K.; Yanagida, T.; Kaji, N.; et al. Discriminating single-bacterial shape using low-aspect-ratio pores. *Sci. Rep.* **2017**, *7*, 1–9. [[CrossRef](#)]
3. Yusko, E.C.; Bruhn, B.R.; Eggenberger, O.; Houghtaling, J.; Rollings, R.C.; Walsh, N.C.; Nandivada, S.; Pindrus, M.; Hall, A.R.; Sept, D.; et al. Real-time shape approximation and fingerprinting of single proteins using a nanopore. *Nat. Nanotechnol.* **2017**, *12*, 360–367. [[CrossRef](#)]
4. Ryuzaki, S.; Tsutsui, M.; He, Y.; Yokota, K.; Arima, A.; Morikawa, T.; Taniguchi, M.; Kawai, T. Rapid structural analysis of nanomaterials in aqueous solutions. *Nanotechnology* **2017**, *28*, 155501. [[CrossRef](#)]
5. Arjmandi, N.; Van Roy, W.; Lagae, L.; Borghs, G. Measuring the Electric Charge and Zeta Potential of Nanometer-Sized Objects Using Pyramidal-Shaped Nanopores. *Anal. Chem.* **2012**, *84*, 8490–8496. [[CrossRef](#)] [[PubMed](#)]
6. Zheng, Y.; Nguyen, J.; Wang, C.; Sun, Y. Electrical measurement of red blood cell deformability on a microfluidic device. *Lab. Chip.* **2013**, *13*, 3275–3283. [[CrossRef](#)] [[PubMed](#)]
7. Darvish, A.; Goyal, G.; Aneja, R.; Sundaram, R.V.K.; Lee, K.; Ahn, C.W.; Kim, K.-B.; Vlahovska, P.M.; Kim, M.J. Nanoparticle mechanics: Deformation detection via nanopore resistive pulse sensing. *Nanoscale* **2016**, *8*, 14420–14431. [[CrossRef](#)] [[PubMed](#)]
8. Wanunu, M. Nanopores: A journey towards DNA sequencing. *Phys. Life Rev.* **2012**, *9*, 125–158. [[CrossRef](#)] [[PubMed](#)]

9. Yokota, K.; Hashimoto, M.; Kajimoto, K.; Tanaka, M.; Murayama, S.; Tsutsui, M.; Nakajima, Y.; Taniguchi, M.; Kataoka, M. Effect of Electrolyte Concentration on Cell Sensing by Measuring Ionic Current Waveform through Micropores. *Biosensors* **2021**, *11*, 78. [[CrossRef](#)]
10. Fusco, V.; Quero, G.M.; Stea, G.; Morea, M.; Visconti, A. Novel PCR-based identification of *Weissella confusa* using an AFLP-derived marker. *Int. J. Food Microbiol.* **2011**, *145*, 437–443. [[CrossRef](#)]
11. Runggrasamee, W.; Tosukhowong, A.; Klanchui, A.; Maibunkaew, S.; Plengvidhya, V.; Karoonuthaisiri, N. Development of bacteria identification array to detect lactobacilli in Thai fermented sausage. *J. Microbiol. Methods* **2012**, *91*, 341–353. [[CrossRef](#)]
12. Shinohara, Y.; Kurniawan, Y.N.; Sakai, H.; Magarifuchi, T.; Suzuki, K. Nanopore based sequencing enables easy and accurate identification of yeasts in breweries. *J. Inst. Brew.* **2021**, *127*, 160–166. [[CrossRef](#)]
13. Bokulich, N.A.; Bamforth, C.W. The Microbiology of Malting and Brewing. *Microbiol. Mol. Biol. Rev.* **2013**, *77*, 157–172. [[CrossRef](#)] [[PubMed](#)]
14. Pham, T.; Wimalasena, T.T.; Box, W.G.; Koivuranta, K.; Storgards, E.; Smart, K.A.; Gibson, B.R. Evaluation of ITS PCR and RFLP for Differentiation and Identification of Brewing Yeast and Brewery ‘Wild’ Yeast Contaminants. *J. Inst. Brew.* **2011**, *117*, 556–568. [[CrossRef](#)] [[PubMed](#)]
15. Kopecká, J.; Němec, M.; Matoulkova, D. Comparison of DNA-based techniques for differentiation of production strains of ale and lager brewing yeast. *J. Appl. Microbiol.* **2016**, *120*, 1561–1573. [[CrossRef](#)]
16. Sherman, F. Getting Started with Yeast. *Methods Enzymol.* **1991**, *194*, 3–21. [[PubMed](#)]
17. Smeets, R.M.M.; Keyser, U.; Dekker, N.; Dekker, C. Noise in solid-state nanopores. *Proc. Natl. Acad. Sci. USA* **2008**, *105*, 417–421. [[CrossRef](#)]
18. Pischel, D.; Buchbinder, J.H.; Sundmacher, K.; Lavrik, I.N.; Flassig, R.J. A guide to automated apoptosis detection: How to make sense of imaging flow cytometry data. *PLoS ONE* **2018**, *13*, e0197208. [[CrossRef](#)] [[PubMed](#)]
19. Fraley, C.; Raftery, A.E. Model-Based Clustering, Discriminant Analysis, and Density Estimation. *J. Am. Stat. Assoc.* **2002**, *97*, 611–631. [[CrossRef](#)]
20. Wernecke, K.-D. Discriminant Analysis. In *Wiley Encyclopedia of Clinical Trials*; D’Agostino, R.B., Sullivan, L., Massaro, J., Eds.; John Wiley & Sons Inc.: Hoboken, NJ, USA, 2007; pp. 1–19.
21. Schoch, R.B.; Han, J.; Renaud, P. Transport phenomena in nanofluidics. *Rev. Mod. Phys.* **2008**, *80*, 839–883. [[CrossRef](#)]
22. Ng, B.; Barry, P.H. The measurement of ionic conductivities and mobilities of certain less common organic ions needed for junction potential corrections in electrophysiology. *J. Neurosci. Methods* **1995**, *56*, 37–41. [[CrossRef](#)]
23. Lide, D.R. *CRC Handbook of Chemistry and Physics*, 84th ed.; CRC Press: Boca Raton, FL, USA, 2003–2004.
24. Grahame, D.C. The Electrical Double Layer and the Theory of Electrocapillarity. *Chem. Rev.* **1947**, *41*, 441–501. [[CrossRef](#)] [[PubMed](#)]
25. Hayashida, T.; Yokota, K.; Murayama, S.; Arima, A.; Tsutsui, M.; Taniguchi, M. Tailoring Dielectric Surface Charge via Atomic Layer Thickness. *ACS Appl. Mater. Interfaces* **2019**, *12*, 5025–5030. [[CrossRef](#)] [[PubMed](#)]
26. Ohshima, H. Approximate analytic expressions for the electrophoretic mobility of spheroidal particles. *Electrophoresis* **2021**, *42*, 1003–1009. [[CrossRef](#)]
27. Beckert, S.F.; Domeneghetti, G.; Bond, D. Using historical results obtained in the tensile tests for Type A evaluation of uncertainty. *Measurement* **2014**, *51*, 420–428. [[CrossRef](#)]
28. He, Y.; Tsutsui, M.; Fan, C.; Taniguchi, M.; Kawai, T. Controlling DNA Translocation through Gate Modulation of Nanopore Wall Surface Charges. *ACS Nano* **2011**, *5*, 5509–5518. [[CrossRef](#)] [[PubMed](#)]
29. Wang, J.; Ma, J.; Ni, Z.; Zhang, L.; Hu, G. Effects of access resistance on the resistive-pulse caused by translocating of a nanoparticle through a nanopore. *RSC Adv.* **2014**, *4*, 7601–7610. [[CrossRef](#)]
30. Brauer, M.J.; Huttenhower, C.; Airoidi, E.M.; Rosenstein, R.; Matese, J.C.; Gresham, D.; Boer, V.M.; Troyanskaya, O.G.; Botstein, D. Coordination of Growth Rate, Cell Cycle, Stress Response, and Metabolic Activity in Yeast. *Mol. Biol. Cell* **2008**, *19*, 352–367. [[CrossRef](#)]
31. Porro, D.; Vai, M.; Vanoni, M.; Alberghina, L.; Hatzis, C. Analysis and modeling of growing budding yeast populations at the single cell level. *Cytom. Part A* **2009**, *75*, 114–120. [[CrossRef](#)]
32. Ohnuki, S.; Enomoto, K.; Yoshimoto, H.; Ohya, Y. Dynamic changes in brewing yeast cells in culture revealed by statistical analyses of yeast morphological data. *J. Biosci. Bioeng.* **2014**, *117*, 278–284. [[CrossRef](#)]